Supplemental Material for "Transition magnon modes in thin ferromagnetic nanogratings."

S. M. Kukhtaruk,[1,2] A. W. Rushforth,[3] F. Godejohann,[1] A. V. Scherbakov,[1] and M. Bayer[1]

[1] *Experimentelle Physik 2, Technische Universität Dortmund, Otto-Hahn-Str. 4a, 44227 Dortmund, Germany.*

[2] *Department of Theoretical Physics, V.E. Lashkaryov Institute of Semiconductor Physics, 03028 Kyiv, Ukraine.*

[3] *School of Physics and Astronomy, University of Nottingham, Nottingham NG7 2RD, United Kingdom.*

I. STATIC DEMAGNETIZING FIELD OF THE NANOGRATINGS

The nonzero components of $\mathbf{H}_{\rm d}^0$ are shown in Fig. S1 for several important directions of $H_{\rm ext}$. As one can see, both components of $\mathbf{H}_{\rm d}^0$ increase with increasing $\varphi_{\rm H}$. For the case of $\varphi_{\rm H} = 90^\circ$ the arrows of the demagnetizing vector field are introduced. Figure S1(a) shows that $H_{{\rm d},x}^0$ is negative in the wire region and positive in the groove region of the NG, which considerably affects the orientation of the magnetization. It is worth emphasizing that the demagnetizing field is nonzero outside the nanograting.

The symmetry of $\mathbf{H}_{\rm d}^0$ with respect to the center of the NG wire region for the $x \to -x$ operation in the steady-state is given by Eq. 4 of the main text. The demagnetizing field imposes different symmetry for the in-plane and out-of-plane magnetization components. Moreover, the symmetry of the i-th component of the magnetization reflects the symmetry of the i-th non-zero component of the demagnetizing field ($i = x, y, z$). In the case of an in-plane $\mathbf{H}_{\rm ext}$, $m_x^0(x, z)$ and $m_z^0(x, z)$ are even and odd functions, respectively (see below). Furthermore, the numerator of the integrand in Eq. 4 consists of the odd functions $m_x^0(x - x')$ and $m_z^0(z - z')$ (one needs to change also $x' \to -x'$). Thus, $H_{{\rm d},x}^0$ is an even, and $H_{{\rm d},z}^0$ is an odd function, respectively. Similarly, one obtains opposite symmetry properties if the magnetization is parallel to the z-direction. In the case of an arbitrary out-of-plane orientation of the magnetization, both $\mathbf{m}^0$ and $\mathbf{H}_{\rm d}^0$ are neither symmetric nor antisymmetric functions.

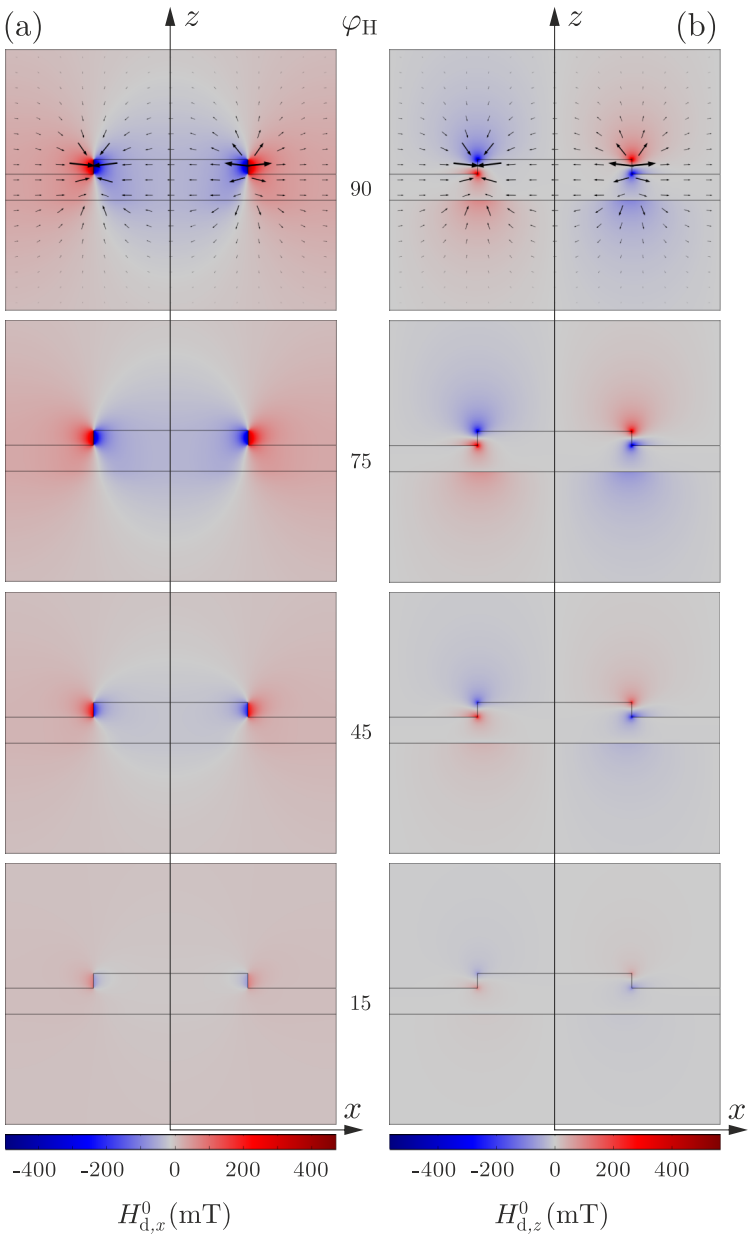

Figure S1. Spatial distributions of the (a) x-components and (b) z-components of the static demagnetizing field $\mathbf{H}_\mathrm{d}^0$ for different directions of $\mathbf{H}_\mathrm{ext}$ at $H_\mathrm{ext} = 200$ mT. The values of φ_H are shown in between (a) and (b) in degrees. In the case of $\varphi_\mathrm{H} = 90°$ arrows represent the demagnetizing vector field. The length of the arrows is proportional to $|\mathbf{H}_\mathrm{d}^0|$ in the center of each arrow.

II. MAGNONS IN NANOGRATINGS FOR DAMON-ESHBACH AND BACKWARD-VOLUME GEOMETRIES

The magnetic field dependencies of the magnon frequencies in nanogratings for both the backward-volume (BV) and Damon-Eshbach (DE) geometries have been already reported in [S1]. In this work, we complement these dependencies by additional antisymmetric magnon modes which cannot be accessed using a symmetric excitation and detection scheme [S1], and higher order modes. For the calculations, all parameters are chosen as they were introduced in the main

text.

Figure S2(a) shows the magnetic field dependence of the magnon frequencies in the DE geometry, i.e. $\varphi_{\mathrm{H}} = 0°$. The presented dependence is similar as for the magnon modes in thin ferromagnetic films for magnetization directions close to the easy axis, because the static demagnetizing field is zero [S1, S2] (see also the Sec. II in the main text).

The magnetic field dependence of the magnon frequencies in the BV geometry ($\varphi_{\mathrm{H}} = 90°$) is shown in Fig. S2(b). The corresponding inset shows the magnetic field dependence of the average steady-state in-plane magnetization angle $\overline{\varphi}_{\mathrm{M}}$, indicating the saturation magnetic field at ≈ 73 mT. For H_{ext} smaller than the saturation magnetic field, one can observe a complicated non-monotonic behavior with magnon-magnon interaction and corresponding avoided crossings. For $H_{\mathrm{ext}} > 73$ mT the behavior is much simpler and in most cases the magnon frequencies monotonically grow with increasing H_{ext}.

Figures S3(a), (b) show the results of micromagnetic simulations for the DE geometry ($\varphi_{\mathrm{H}} = 0°$). For this field direction, $\overline{\varphi}_{\mathrm{M}} = \varphi_{\mathrm{H}}$, because the static demagnetizing field is zero [S2]. From Fig. S3(a) one can see that all magnon branches are nonreciprocal, i.e. $\omega(k_x) \neq \omega(-k_x)$, except for the ground one. Moreover, indirect band gaps arise.

Figure S3(b) shows magnon modes' spatial profiles which correspond to the center of the Brillouin zone at $k_x = 0$. The ground magnon mode is quasiuniform. The next two modes are symmetric and antisymmetric magnon modes with $k_x = 2\pi/d$. The following modes are higher-order magnon modes. Magnon modes with wave vectors corresponding to the center of the Brillouin zone are propagating waves. Their group velocities $v_{\mathrm{g}} = \frac{d\omega}{dk_x}$ are defined by the slopes of the dispersion curves. As an example, see Supplemental Video I, where the third mode corresponding to $k_x = 0$ and possessing a negative group velocity, is visualized and its motion in the negative x-direction is clearly seen.

Figures S3(c), (d) show magnon modes' dispersion curves and their spatial profiles in the BV geometry ($\varphi_{\mathrm{H}} = 90°$). One can see, that this case drastically differs from the case of the DE geometry. In Fig. S3(c), all modes are reciprocal. The first eleven dispersion branches are nearly

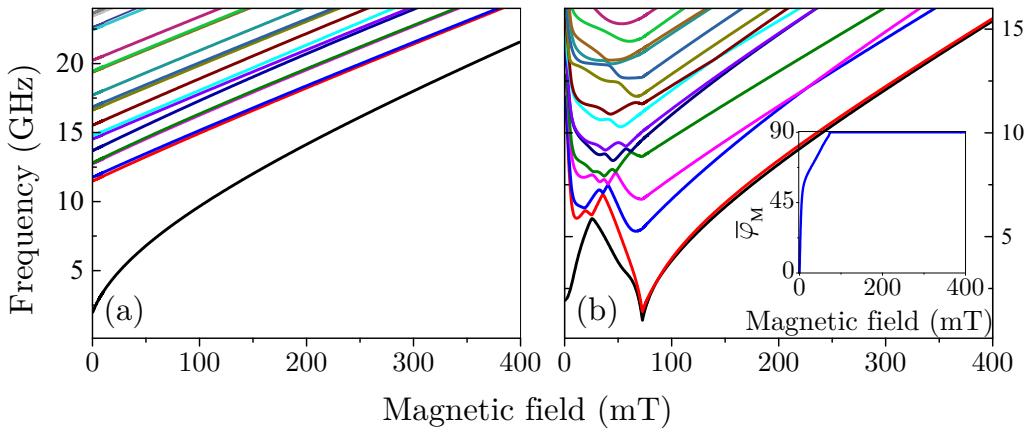

Figure S2. Magnetic field dependencies of the magnon frequencies for the case of (a) the DE geometry ($\varphi_{\mathrm{H}} = 0°$) and (b) the BV geometry ($\varphi_{\mathrm{H}} = 90°$). The inset in (b) shows the magnetic field dependence of the average steady-state in-plane magnetization angle $\overline{\varphi}_{\mathrm{M}}$. Note, that the vertical scales in (a) and (b) are different. The magnon mode branches correspond to the center of the Brillouin zone. The color schemes of the lines here, below and in the main text are the same.

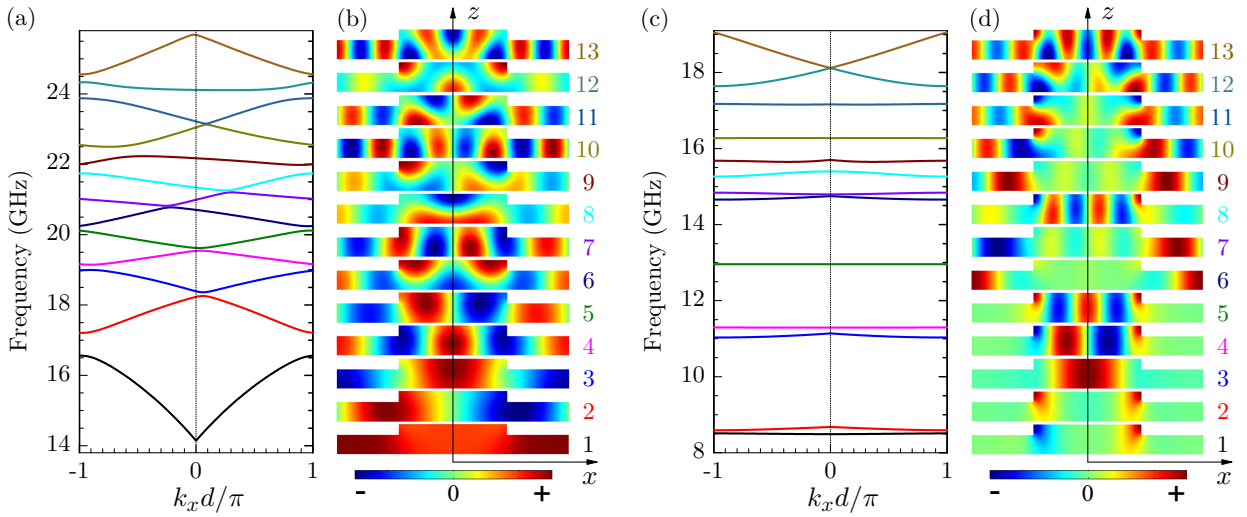

Figure S3. Magnon dispersions and mode profiles at $H_{\text{ext}} = 200\,\text{mT}$ in (a), (b) the DE geometry and (c), (d) the BV geometry. (a), (c) Magnon dispersion curves. The vertical dotted line in (a), (c) at $k_x = 0$ indicates the center of the Brillouin zone. (b), (d) Spatial profiles of the magnon modes at $k_x = 0$ in the unit cell of the NG. The colored numbers correspond to the magnon dispersion branches.

flat [S1, S3]. Moreover, the existence of huge band gaps in their frequency spectrum is worth of mention. The largest three band gaps are between the second and third, fourth and fifth, and fifth and sixth magnon branches possessing values of 2.35 GHz, 1.67 GHz, and 1.7 GHz, respectively.

Figure S3(d) shows magnon modes' spatial profiles which correspond to the center of the Brillouin zone at $k_x = 0$. In the BV geometry all modes are standing waves due to the reciprocal dispersion. The first two modes are antisymmetric and symmetric edge modes. The next three are so-called wire modes. The 6-th and 7-th modes are symmetric and antisymmetric groove modes [S1]. An example of wire mode oscillations can be found in the Supplemental Video II.

The presented results in Fig. S2 are perfectly consistent with previously reported experimental (FMR) and numerical results [S1]. For the DE geometry, Fig. S2(b) has to be compared to Fig. 7 in [S1]. For the case of the BV geometry, Fig. S2(a) has to be compared to Fig. 5(d), (h) in [S1]. Note, that in this work the number of lines is larger than in [S1], because Fig. S2 shows both symmetric and antisymmetric magnon modes.

III. SPATIAL FOURIER TRANSFORM OF MAGNON MODES

Figure S4 shows the results of spatial Fourier transforms of the magnon modes' spatial profiles for different directions of the external magnetic field. For instance, Fig. S4(a) for $\varphi_{\text{H}} = 0°$ shows that the value of the Fourier amplitude at $n = 0$ is much larger than the values for other n. That is, this mode is a quasiuniform magnon mode. Similarly, Figs. S4 (b), (c) for $\varphi_{\text{H}} = 0$ show modes with $n = 1$ and $n = 2$, respectively. In the BV geometry, the magnon modes are characterized by several values of n. In the transition range, i.e. from $\varphi_{\text{H}} \approx 50°$ to $\approx 75°$ the spectral composition considerably differs from the spectral composition at $\varphi_{\text{H}} = 90°$. The sharp peaks are caused by magnon-magnon interactions with other magnon modes.

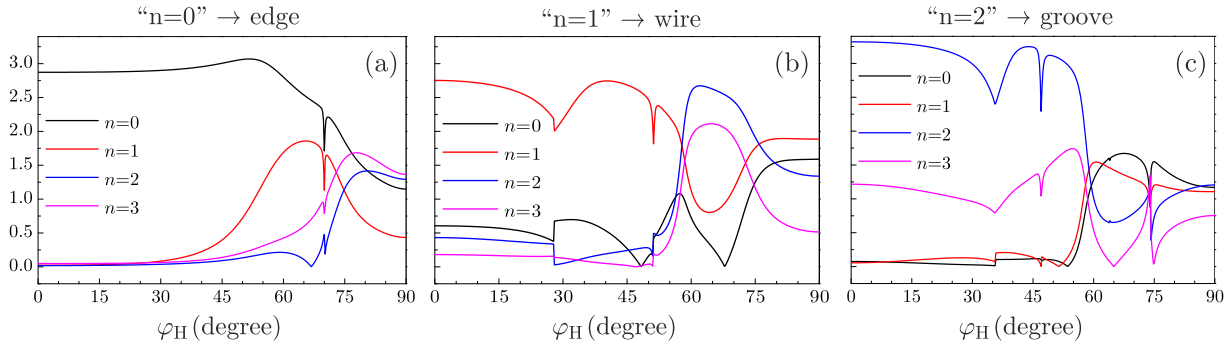

Figure S4. Dependencies of the spatial Fourier amplitudes for the main harmonics on the external magnetic field direction for the transition of (a) "$n = 0$ mode" to the edge mode; (b) "$n = 1$ mode" to the wire mode; (c) "$n = 2$ mode" to the groove mode.

IV. VERIFICATION OF MICROMAGNETIC SIMULATIONS USING COMSOL MULTIPHYSICS

In reference [S4] five μMAG standard problems of micromagnetics can be found. Among all of them, problem #4 deals with the case of a spatially nonhomogeneous, time-dependent magnetization precession in a thin Permalloy plate. Due to the link to the treated system in this work, in the following, the problem is formulated and solved using COMSOL Multiphysics® [S5] (Comsol). In order to verify the accuracy of the solved problem using Comsol, a comparison with different solutions given in [S4] is discussed.

We want to emphasize, that we are not claiming the novelty of utilizing Comsol for micromagnetic simulations (see e.g. [S6, S7]). However, as far as micromagnetics is not a default module of Comsol we decided to verify our implementation of micromagnetics to Comsol by solving the standard micromagnetic problems.

The object of our study is given by the Permalloy plate, which is illustrated in Fig. S5. The used parameters are $L = 500$ nm, $d = 125$ nm and $t = 3$ nm. We take the same Permalloy material parameters as used in [S4] only in this section of the Supplemental Material. It is important to emphasize that these parameters are different from the values in reference [S1], which have been used in the main text. Hence, the exchange stiffness constant is $D = 3.25 \cdot 10^{-17}$ Tm^2. The saturation magnetization is $M_s = 1.0053$ T, and the Gilbert damping constant is $\alpha = 0.02$.

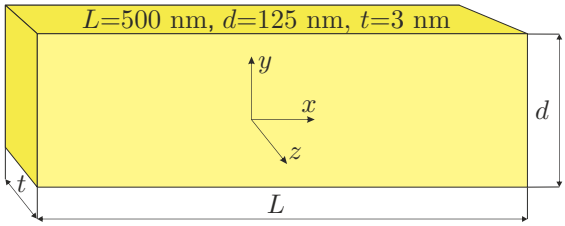

Figure S5. Sketch of the geometry of the micromagnetic problem (not to scale!).

The first part of the solution of problem #4 is given by the calculation of the so-called s-state, which is the specific steady-state spatial distribution of the magnetization (see Fig. S6(a)). In order to do so, a saturating magnetic field is applied along the [111]-crystallographic direction and,

subsequently, slowly decreased to zero. As one can see in Fig. S6, the calculated s-state using Comsol looks very similar to the results taken from [S4] (see Fig. S6(b)). The resulting s-state determines the initial state for the solution of the second part of problem #4, which deals with the time evolution of the magnetization.

For the second part of problem #4, another magnetic field is applied along the opposite direction of the equilibrium magnetization of the s-state in order to change the magnetization orientation. The main aim is to track the time evolution of the magnetization towards the new magnetic field direction [S4]. The applied magnetic field is given by $H_x = -24.6$ mT, $H_y = -4.3$ mT, and $H_z = 0.0$ mT. In other words, the magnetic field strength of ≈ 25 mT is directed 170 degrees counterclockwise relative to the positive x-axis in the x-y plane.

In this paragraph, we present the details of the calculation in Comsol which could be useful for Comsol users. For the magnetic field calculation we used the "AC/DC" module ("Magnetic Fields, No Currents"). The Landau-Lifshits-Gilbert equation was implemented using the basic module of Comsol i.e. "Mathematics" ("Coefficient form PDE"). We introduce an air sphere of 2 μm radius around the Permalloy plate with a 200-nm thick external layer of "infinite element domain". The magnetic scalar potential on the surface of the sphere is set to zero. The maximum element size in the plate is set to 5 nm. For the sphere, we choose an "extremely coarse" mesh. We used the quartic Lagrange discretization in the Coefficient form PDE and quadratic in the "Magnetic Fields, No Currents". The maximum time step is taken as 0.5 ps.

Figure S7 summarizes the calculated time-dependent spatially averaged magnetization components by our and other groups. Fig. S7(a) shows the comparison of the results obtained using Comsol (lines) and using a finite difference software developed by E. Martinez, L. Torres and L. Lopez-Diaz (dots). One can see a very good agreement between the calculated lines and dots. Another comparison of the results using Comsol and using the finite difference software developed by J. L. Martins and T. Rocha is presented in Fig. S7(b). In this case, perfect agreement between both calculations is observed. The discrepancy between the different calculations is due to the fact that the exact analytical solution of the considered problem is unknown. Thus, different approaches, different mesh sizes, etc., give slightly different results.

We want to emphasize, that the calculated amplitude of precession is on the order of the saturation magnetization (see Fig. S7), which is much larger than in usual experiments investigating

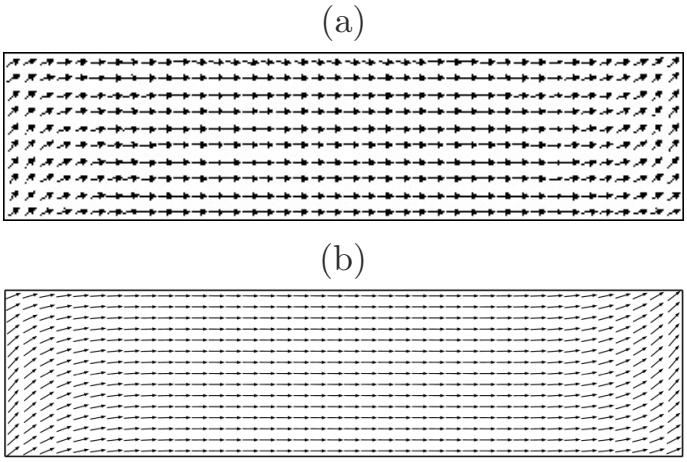

Figure S6. Steady-state spatial distribution of the magnetization in the s-state: (a) taken from [S4]; (b) Comsol calculations.

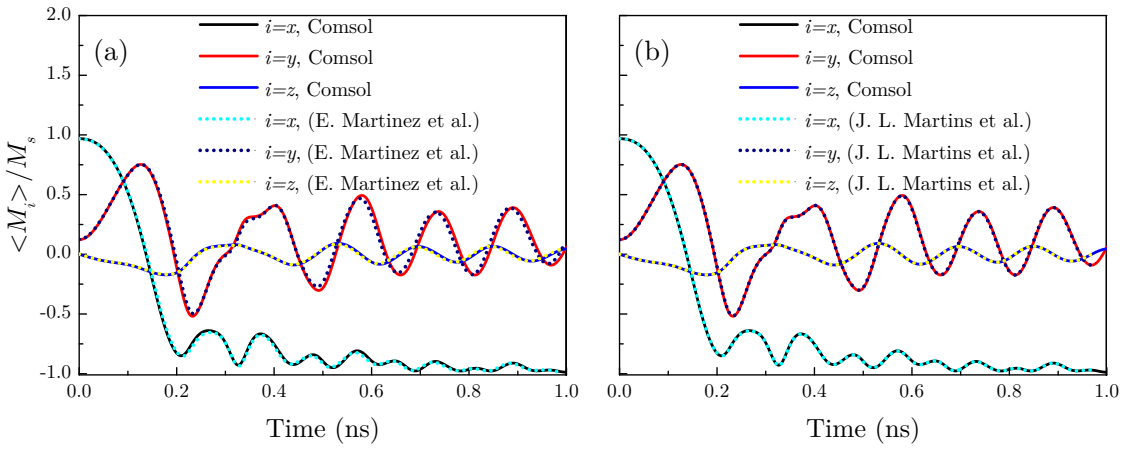

Figure S7. Comparison of results of micromagnetic calculations which were obtained with Comsol and results from the groups of (a) E. Martinez et al. (data for 2.5 nm mesh size [S4]) and (b) J. L. Martins et al. (data for 1 nm mesh size [S4]).

magnons (see e.g. [S8–S11]). Hence, the three-dimensional problem #4 is strongly nonlinear and reflects a case, which is much more complicated than the simulation of magnons in effectively two-dimensional gratings with precession amplitudes much smaller than M_s.

The last validation of the solution of problem #4 is provided by the comparison of the spatial distribution of the magnetization at the time, when the x-component of the spatially averaged magnetization first crosses zero (≈ 0.1375 ns). In Fig. S8(a) one can see the spatial distribution which was calculated by M. J. Donahue and D. G. Porter, using the OOMMF eXtensible solver [S4], while Fig. S8(b) shows the spatial distribution of the magnetization using Comsol. Besides the different colors, there is good agreement between both calculated distributions.

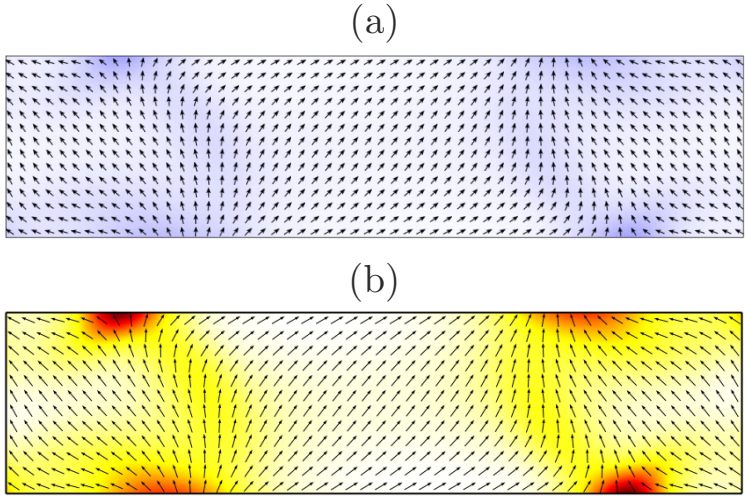

Figure S8. Spatial distribution of the magnetization at the time = 0.1375 ns (see Fig. S7). Distribution (a) is calculated by M. J. Donahue et al., using the OOMMF software, and distribution (b) is calculated using Comsol. The background color indicates the z component of the magnetization.

[S1] M. Langer, R. A. Gallardo, T. Schneider, S. Stienen, A. Roldán-Molina, Y. Yuan, K. Lenz, J. Lindner, P. Landeros, and J. Fassbender, Phys. Rev. B **99**, 024426 (2019).

[S2] I. Lisenkov, D. Kalyabin, S. Osokin, J. W. Klos, M. Krawczyk, and S. Nikitov, J. Magn. Magn. Mater. **378**, 313 (2015).

[S3] R. A. Gallardo, T. Schneider, A. Roldán-Molina, M. Langer, J. Fassbender, K. Lenz, J. Lindner, and P. Landeros, Phys. Rev. B **97**, 144405 (2018).

[S4] μMAG, Micromagnetic Modeling Activity Group, www.ctcms.nist.gov/∼rdm/mumag.org.html.

[S5] COMSOL Multiphysics® v. 5.4. www.comsol.com. COMSOL AB, Stockholm, Sweden.

[S6] M. Mruczkiewicz, M. Krawczyk, V. K. Sakharov, Y. V. Khivintsev, Y. A. Filimonov, and S. A. Nikitov, J. Appl. Phys. **113**, 093908 (2013).

[S7] J. Rychły, P. Gruszecki, M. Mruczkiewicz, J. W. Kłos, S. Mamica, and M. Krawczyk, Low Temperature Physics **41**, 745 (2015).

[S8] M. van Kampen, C. Jozsa, J. T. Kohlhepp, P. LeClair, L. Lagae, W. J. M. de Jonge, and B. Koopmans, Phys. Rev. Lett. **88**, 227201 (2002).

[S9] V. N. Kats, T. L. Linnik, A. S. Salasyuk, A. W. Rushforth, M. Wang, P. Wadley, A. V. Akimov, S. A. Cavill, V. Holy, A. M. Kalashnikova, and A. V. Scherbakov, Phys. Rev. B **93**, 214422 (2016).

[S10] A. S. Salasyuk, A. V. Rudkovskaya, A. P. Danilov, B. A. Glavin, S. M. Kukhtaruk, M. Wang, A. W. Rushforth, P. A. Nekludova, S. V. Sokolov, A. A. Elistratov, D. R. Yakovlev, M. Bayer, A. V. Akimov, and A. V. Scherbakov, Phys. Rev. B **97**, 060404(R) (2018).

[S11] A. V. Scherbakov, A. P. Danilov, F. Godejohann, T. L. Linnik, B. A. Glavin, L. A. Shelukhin, D. P. Pattnaik, M. Wang, A. W. Rushforth, D. R. Yakovlev, A. V. Akimov, and M. Bayer, Phys. Rev. Applied **11**, 031003 (2019).